Journal of the European Ceramic Society xxx (xxxx) xxx–xxx

Contents lists available at ScienceDirect

Journal of the European Ceramic Society

journal homepage: www.elsevier.com/locate/jeurceramsoc

Original Article

The impact of heat-treatment protocol on the grain size and ionic conductivity of NASICON glass-ceramics

Adriana M. Nieto-Muñoz[a], Jairo F. Ortiz-Mosquera[a,*], Ana C.M. Rodrigues[b]

[a] Programa de Pós-graduação em Ciência e Engenharia de Materiais, Universidade Federal de São Carlos, CP 676, 13565-905, São Carlos, SP, Brazil
[b] Departamento de Engenharia de Materiais, Universidade Federal de São Carlos, CP 676, 13565-905, São Carlos, SP, Brazil

ARTICLE INFO

Keywords:
Grain size effect
Brick layer model
NASICON
Glass-ceramics
Grain boundary conductivity

ABSTRACT

$Na_2AlTi(PO_4)_3$ (NATP) and $Na_{1.8}Al_{0.8}Ge_{1.2}(PO_4)_3$ (NAGP) NASICON (Na-Superionic Conductor) glass-ceramics are obtained by applying different single (SHT) and double (DHT) heat treatments on the respective precursor glass to evaluate its effect on the microstructure and in turn, on the total ionic conductivity. The grain and grain boundary contributions are also analyzed in the NATP composition. SHT with longer crystallization times favors the development of well-defined grains in both compositions and also promotes the grain growth in NAGP samples. This behavior causes a decrease in the activation energy of the grain boundary, which enhances the total ionic conductivity. Regarding DHT samples, microstructure with larger grains and higher ionic conductivity were obtained with shorter nucleation times for NATP and NAGP compositions. Finally, the microstructural variation generated by the different thermal treatments causes the total conductivity to increase up to two times.

1. Introduction

Various studies have demonstrated that the glass-ceramic route is a promising synthesis method as it has advantages compared to the conventional synthesis processes by solid-state reaction followed by sintering [1–6]. Among these advantages, the following can be mentioned: the easy synthesis of materials with lower porosity; the design and control of the final microstructure by suitable heat treatments; and the elaboration of pieces in different sizes and shapes. Furthermore, the crystallization of parent glasses is performed at moderate temperatures when compared to ceramic sintering temperatures (> 1000 °C). As known, this synthesis route consists of crystallizing a precursor glass by controlled heat treatment. The final material obtained after crystallization treatment is called glass-ceramic, regardless of the crystallized volume fraction achieved [7].

The glass to glass-ceramic transformation process consists of two steps: nucleation and crystal growth. During the nucleation step, the glassy material is heated at a certain temperature (nucleation temperature, T_n) in order to promote the generation of embryos, i.e., a small cluster of atoms in the vitreous matrix. The embryos or clusters that are larger than a critical size, are stable and called crystalline nuclei, while those with smaller radii, i.e., unstable clusters, dissolve in the glassy material [8,9]. However, it should be mentioned that some nuclei can also be generated during the cooling of the melting liquid in the synthesis of the precursor glass which are called the athermic nuclei [10]. In the second or crystal growth step, nuclei generated either in the first nucleation stage or during cooling (the athermic nuclei) are grown. Crystallization heat treatments of a precursor glass can be called a single heat treatment (SHT) when the crystal growth occurs only from the athermic nuclei and double heat treatment (DHT) when the glass is subjected to a nucleation heat treatment previous to the crystal growth one.

Microstructural characteristics of glass-ceramics depend greatly on nucleation and grain growth steps. For example, to synthesize glass-ceramics with small grain sizes, the application of heat treatments with longer nucleation times on the precursor glass is required to promote higher nucleus density. In the case of bulk homogeneous nucleation, the grain size is limited during the crystal growth step, thus resulting in the formation of small grains. Otherwise, glass-ceramics with large grains are expected when short nucleation times are used, leading to small nuclei density and also when only athermic nuclei are grown. These facts are relevant since microstructural control plays an important role in the properties of materials, including ionic conductivity in solid electrolytes [3,4,6,11].

The solid electrolyte is one of the fundamental components of solid-state batteries, and its main function is to transport ionic species between the electrodes of the electrochemical cell. The optimization of the microstructure of this cell component has been the subject of

* Corresponding author.
E-mail addresses: adrianaanietomunoz@gmail.com (A.M. Nieto-Muñoz), felipeortiz980@gmail.com (J.F. Ortiz-Mosquera), acmr@ufscar.br (A.C.M. Rodrigues).

https://doi.org/10.1016/j.jeurceramsoc.2020.05.026
Received 30 March 2020; Received in revised form 9 May 2020; Accepted 10 May 2020

several researches in an attempt to improve its ionic conductivity [6,12,13], which can contribute to the decrease of internal resistance (ohmic loss) of the battery [14,15]. The $Li_{1+x}Al_xM_{2-x}(PO_4)_3$ (M = Ge, Ti) NASICON compounds stand out among Li^+-ion conducting solid electrolytes due to their high ionic conductivities at low temperatures (< 60 °C) [15]. Cruz et al. [4] and Narváez-Semanate et al. [6] obtained glass-ceramics with different microstructures from these NASICON series by applying different crystallization treatments (SHT and DHT). Both authors confirmed that the increase in average grain size enhances the ionic conductivity of samples. In addition, Narváez-Semanate et al. also showed evidence that $Li_{1.3}Al_{0.3}Ti_{1.7}(PO_4)_3$ samples crystallized by DHT exhibited higher values of electrical conductivity than those obtained by SHT performed at the same growth temperature of DHT and with the same grain size. According to the authors, the highest degree of crystallinity achieved in the glass-ceramics obtained by double heat treatments was responsible for the increase in ionic conductivity. It follows from the above that different heat treatments for glass crystallization lead to glass-ceramics with different microstructures and in turn, the electrical properties of the materials can be optimized.

On the other hand, several studies point out to sodium-based batteries being a potential option for replacing lithium-ion batteries in the future (e.g., stationary storage devices) due to the wide availability and low cost of sodium compared to lithium, as well as the high Na^+ redox potential [15–17]. Following this idea, we synthesized NASICON glass-ceramics of $Na_2AlTi(PO_4)_3$ (NATP) and $Na_{1.8}Al_{0.8}Ge_{1.2}(PO_4)_3$ (NAGP) compositions applying single and double heat treatments to their respective precursor glasses. NATP and NAGP compounds correspond to the most conductive compositions of the $Na_{1+x}Al_xM_{2-x}(PO_4)_3$ (M = Ti, Ge) NASICON family [5,18], which is a sodium-ion conductive series analogous to that NASICON series studied by Cruz et al. [4] and Narváez-Semanate et al. [6]. To the best of our knowledge, there are no reports on microstructural changes promoted by using different crystallization heat treatments and their influence on electrical properties of these two glass-ceramics NASICON series.

In this study, we performed differential scanning calorimetry (DSC) to determine the appropriate temperatures for crystallizing the precursor glass and X-ray powder diffraction to verify the formation of the NASICON crystalline phase after heat treatments. Afterwards, we presented a detailed analysis of the microstructural and electrical evolution as revealed by scanning electronic microscopy (SEM) and impedance spectroscopy (IS), respectively.

2. Experimental procedure

2.1. Synthesis of precursor glasses

$Na_2AlTi(PO_4)_3$ and $Na_{1.8}Al_{0.8}Ge_{1.2}(PO_4)_3$ precursor glasses with molar composition $25Na_2O–12.5Al_2O_3–25TiO_2–37.5P_2O_5$ and $22.5Na_2O–10Al_2O_3–30GeO_2–37.5P_2O_5$ respectively, were synthesized following the experimental procedure and using the same reagent grade chemicals as described in our previous work [5,18]. Accordingly, adequate quantities of raw materials to obtain 20 g batches of the precursor glasses were homogenized in a rotary jar mill for 2 h with alumina balls. The mixed powders were heated from room temperature to 700 °C (10 °C/min heating rate) in a platinum crucible and maintained at this last temperature for 1 h to promote the decomposition of Na_2CO_3 and $(NH_4)_2HPO_4$ reagents and thereby allow the release of CO_2, NH_3 and H_2O gases. After the calcination treatment, the temperature was raised with a heating rate of 20 °C/min to 1450 °C and 1250 °C for the NATP and NAGP, respectively. The melting time was 30 min for both compositions. The molten liquid was cooled by the conventional splat cooling technique. Thus, vitreous plates with a thickness of 1–2 mm were obtained. After the synthesis of glassy material, residual thermal stresses were removed by annealing at a temperature of 40 °C below the glass transition temperature (T_g, determined by DSC as indicated in Fig. 1) for 2 h. Then, the samples were slowly cooled to room temperature.

2.2. Thermal analysis and temperature of maximum nucleation rate (T_n^{max}) of glasses

The thermal analysis for the determination of the characteristic temperatures (T_x: crystallization temperature, T_g: glass transition temperature and T_m: melting temperature) of the precursor glasses was performed by differential scanning calorimetry (DSC- Netzsch 404) using a platinum crucible in air atmosphere with a heating rate of 10 °C/min, in a temperature range from 30 °C to 1000 °C and 1250 °C for NATP and NAGP, respectively.

The temperature of the maximum nucleation rate (T_n^{max}) of NATP and NAGP precursor glasses was determined according to the method proposed by Ray et al. [19], which has already been applied to other precursor glasses of NASICON compounds [4]. This technique consists of inducing nucleation on the precursor glass at different temperatures around the glass transition temperature (T_g) at a fixed length of time. Then, the temperature of the DSC crystallization peak (T_p) is determined from the DSC thermogram. As shown by Ray et al. [19] and Cruz et al. [4], the T_n^{max} corresponds to the maximum temperature of the $1/T_p$ vs. nucleation temperature plot.

Thus, nucleation heat treatments were performed at five different temperatures ($T_g - 20$, $T_g - 10$, T_g, $T_g + 10$, and $T_g + 20$) on NATP and NAGP samples to determine the T_n^{max}. The duration of nucleation heat treatments was 30 and 180 min for NATP and NAGP, respectively.

2.3. Crystallization of precursor glass: single (SHT) and double (DHT) heat treatments

To obtain the NATP and NAGP glass-ceramics, precursor glasses were subjected to single and double heat treatments. The nucleation and grain growth temperatures, as well as the times used in both heat treatments, are summarized in Table 1. As mentioned earlier, the DHT consists of two steps of crystallization: the first one for nucleus formation and the second one for crystal growth. In this case, we performed the nucleation step at the temperature corresponding to the maximum nucleation rate (T_n^{max}) of the precursor glass in both compositions. The isothermal treatment times for this first step varied from 1 to 12 h for the NATP composition and from 3 to 24 h for the NAGP, as indicated in Table 1. For the crystal growth stage, a heat treatment temperature between the glass transition (T_g) and crystallization (T_x) temperatures (630 °C for NATP and 600 °C for NAGP) was chosen to avoid a rapid crystallization process, thus enabling a better control of the microstructure.

Regarding the SHT (without a previous nucleation stage), the crystallization treatments were made on the precursor glasses at the same temperature used for the crystal growth step of the DHT (see Table 1). The crystallization times for these heat treatments were 1, 3, and 6 h in both compositions. Additionally, SHTs at higher temperatures (700–850 °C) were also performed for 1 h to evaluate the effect of SHT at increased temperatures on microstructural characteristics. All the crystallization treatments (SHT and DHT) to obtain the glass-ceramics were performed in a tubular and vertical electric furnace having a precision of ± 1 °C in the temperature control. It should be noted that the glassy samples were placed in the electric furnace, which was previously equilibrated at the respective target temperature following the crystallization protocol summarized in Table 1. After the nucleation and grain growth step, the samples were removed from the furnace and left to cool to room temperature.

2.4. Characterization of glass-ceramics

X-ray patterns were obtained in the 10° to 80° 2θ range at room temperature using a Rigaku Ultima IV diffractometer with Cu target (K_α wavelength) at 40 kV and 20 mA, employing an integration time and

step size of 0.29 s and 0.02°, respectively. For X-ray analysis, the glass-ceramic samples were previously ground in an agate mortar, and the resultant powders were sifted through a 230 mesh (≤63 μm). Crystallographica Search Match [20] and TOPAS version 6 software [21] were used to index and quantify the crystalline phases, respectively. The crystallographic files (CIF) were extracted from the Inorganic Crystal Structure Database (ICSD) [22] for the Rietveld analysis.

The Archimedes' principle was used to determine the experimental density of the NATP and NAGP single-phase glass-ceramics. As a test to the possible hygroscopicity of samples due to the presence of P_2O_5 in their composition, water ($\rho_{exp\text{-}w}$) and ethanol ($\rho_{exp\text{-}e}$) were used as immersion fluids. Measurements were carried out in a Mettler-Toledo AX-204 analytical lab balance.

The variation of electrical conductivity as a function of frequency and temperature was determined by complex impedance spectroscopy (Novocontrol Alpha-A High-Performance Frequency Analyzer) on parallelepipedal samples with a surface area and thickness of ~6 mm^2 and ~1.5 mm, respectively. Sputtered gold was deposited on both parallel surfaces as a contact electrode. The impedance measurements were performed in the 10 MHz to 0.1 Hz frequency range at temperatures between 50–300 °C.

Finally, images from scanning electron microscopy (Phillips XL30 FEG) were obtained on the fractured surface of the same glass-ceramic samples used in the impedance measurements. Grain size determination was performed by measuring 50 grains from the SEM micrographs of each sample using ImageJ open-source software [23].

3. Results and discussion

3.1. Thermal analysis

Fig. 1 shows the DSC thermograms of the bulk (monolithic) and powder (particle size < 63 μm) samples of the NATP and NAGP

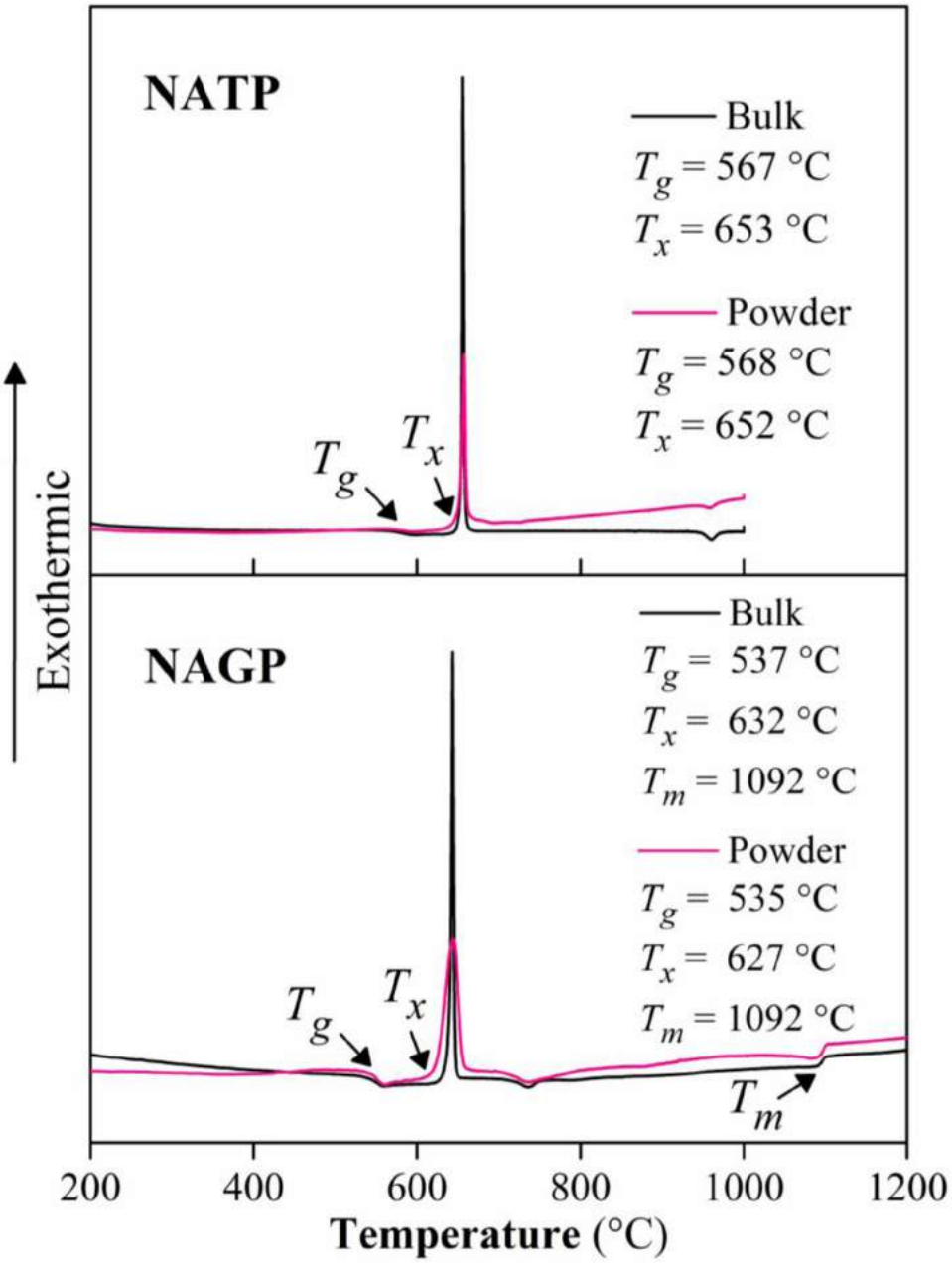

Fig. 1. DSC thermograms of bulk and powder (particle size < 63 μm) samples of NATP and NAGP compositions at a heating rate of 10 °C/min. Characteristic temperatures (T_g, T_x, and T_m) are also indicated.

Table 1
Temperatures and times of the nucleation and grain growth steps in the single (SHT) and double (DHT) heat treatments performed on the NATP and NAGP precursor glasses.

Composition	Heat treatment	Sample	Nucleation		Crystal growth	
			Temperature*(°C)	Time(h)	Temperature(°C)	Time(h)
		S1	–	–	630	1
		S3	–	–	630	3
	SHT	S6	–	–	630	6
		S750	–	–	750	1
NATP		S850	–	–	850	1
(T_g = 567 °C)		D1	577	1	630	1
		D3	577	3	630	1
	DHT	D6	577	6	630	1
		D9	577	9	630	1
		D12	577	12	630	1
		S1	–	–	600	1
	SHT	S3	–	–	600	3
		S6	–	–	600	6
		S700	–	–	700	1
NAGP		D3	547	3	600	1
(T_g = 537 °C)		D6	547	6	600	1
	DHT	D12	547	12	600	1
		D18	547	18	600	1
		D24	547	24	600	1

* Nucleation temperature corresponding to the temperature of the maximum nucleation rate according to DSC analysis.

precursor glasses. DSC curves of both glassy samples exhibit an event in the endothermic direction, characteristic of the glass transition, followed by a single well-defined exothermic peak above 600 °C, which was associated with the crystallization process of the vitreous sample. The crystallization temperature (T_x) was determined from the onset of the crystallization peak, as indicated in Fig. 1, and the T_g temperature was taken at the inflection point of the baseline into the endothermic direction. The characteristic temperatures for the monolith and powered samples of the NATP and NAGP glasses are indicated in Fig. 1.

Moreover, in Fig. 1, it can be seen that the crystallization peaks of the bulk and powder samples coincide for both compositions. This behavior suggests that $Na_2AlTi(PO_4)_3$ and $Na_{1.8}Al_{0.8}Ge_{1.2}(PO_4)_3$ precursor glasses nuclei in volume., i.e., surface crystallization is not predominant in these compositions of glasses [4,5,24]. If surface nucleation were predominant, it is expected that, due to the larger surface area, the crystallization peak of the powder sample would occur at a lower temperature as compared to that of the bulk sample. This result is relevant because it indicates that it is possible to control the microstructure of the material without using nucleating agents, which may affect the crystallized phase stoichiometry. In our previous work [5], we also observed the same DSC behavior in bulk and powder samples of the precursor glasses of the NASICON $Na_{1+x}Al_xGe_{2-x}(PO_4)_3$ series ($0 \leq x \leq 1.0$). Besides, it was also reported for these glasses that the T_{gr} parameter (reduced glass transition temperature, $T_{gr} = T_g / T_m$ (temperatures in K) is lower than 0.6, which is another indicator of homogeneous nucleation [25]. For the NAGP composition ($x = 0.8$) investigated here, $T_{gr} = 0.59$ (Fig. 1). In the case of the NATP precursor glass, it was not possible to calculate the T_{gr} parameter since the melting temperature was not observed at the temperature range analyzed by DSC. The endothermic event before 1000 °C for NATP glass and around 750 °C for the NAGP sample (Fig. 1) is attributed to the beginning of the melting process, i.e., it corresponds to the solidus temperature (T_s) at which the first liquid appears and the solid solution initiates its decomposition. In fact, the grain rounding and intense de-alumination observed in NAGP glass-ceramics, obtained by SHT at temperatures higher than this T_s value [26], also suggest the beginning of the melting process. This solidus temperature has also been observed in other titanium-containing glasses, which also crystallize in the NASICON $NaTi_2(PO_4)_3$ phase [27].

3.2. Determination of the maximum nucleation rate (T_n^{max})

Fig. 2a–b shows the DSC curves obtained for the NATP and NAGP vitreous samples nucleated at $T_g - 20$, $T_g - 10$, T_g, $T_g + 10$ and $T_g + 20$. As can be seen for both compositions, the crystallization peak shifts to lower temperatures as the nucleation temperature increases. According to Ray et al. [19], this behavior is expected since higher heat treatment temperatures (or also, longer nucleation times) promote more nucleation in the glass matrix, and thus the probability of initiating the crystallization by the crystal growth also increases due to an increased density of nuclei.

In addition, no significant variations in the intensity of the crystallization peaks were observed in Fig. 2a–b, despite the temperature difference in the nucleation treatments. Cruz et al. [4] state that this result is due to the fact that the crystal growth rate is negligible in the investigated nucleation temperature range (around T_g).

Following Ray's method, the temperature of the crystallization peak (T_p) was determined from the data shown in Fig. 2a–b, and the inverse of this temperature ($1/T_p$) was plotted as a function of the nucleation temperature (see Fig. 2c–d). Fig. 2c–d shows that there is no significant variation in the temperature of crystallization peak from $T_g + 10$. It suggests that NAGP and NATP samples nucleated at $T_g + 10$ and $T_g + 20$ present a similar quantity of nuclei. In other words, it means that the nuclei saturation in the glass, for that period of time, has been reached at $T_g + 10$ in both compositions. Thus, as shown by Ray et al. [19], we can assume that $T_g + 10$ corresponds to the temperature of the maximum nucleation rate (T_n^{max}). Therefore, the nucleation step of the double heat treatments was performed at 577 °C and 547 °C on the NATP and NAGP precursor glasses, respectively.

3.3. X-ray diffraction and rietveld refinement

The X-ray diffractogram patterns of NAGP and NATP glass-ceramic samples obtained by SHT and DHT are shown in Fig. 3. It is worth noting that the NASICON (ICSD 290802) is the only crystalline phase formed after all the heat treatments performed in the NATP precursor glass, except for those glass-ceramics obtained at temperatures higher than those chosen for growth (> 630 °C). According to Rietveld refinement, a percentage of less than 2 wt% of the $AlPO_4$ spurious phase (ICSD 280307) was formed in the NATP S750 and S850 samples.

Regarding the NAGP glass-ceramics, the NASICON phase with file

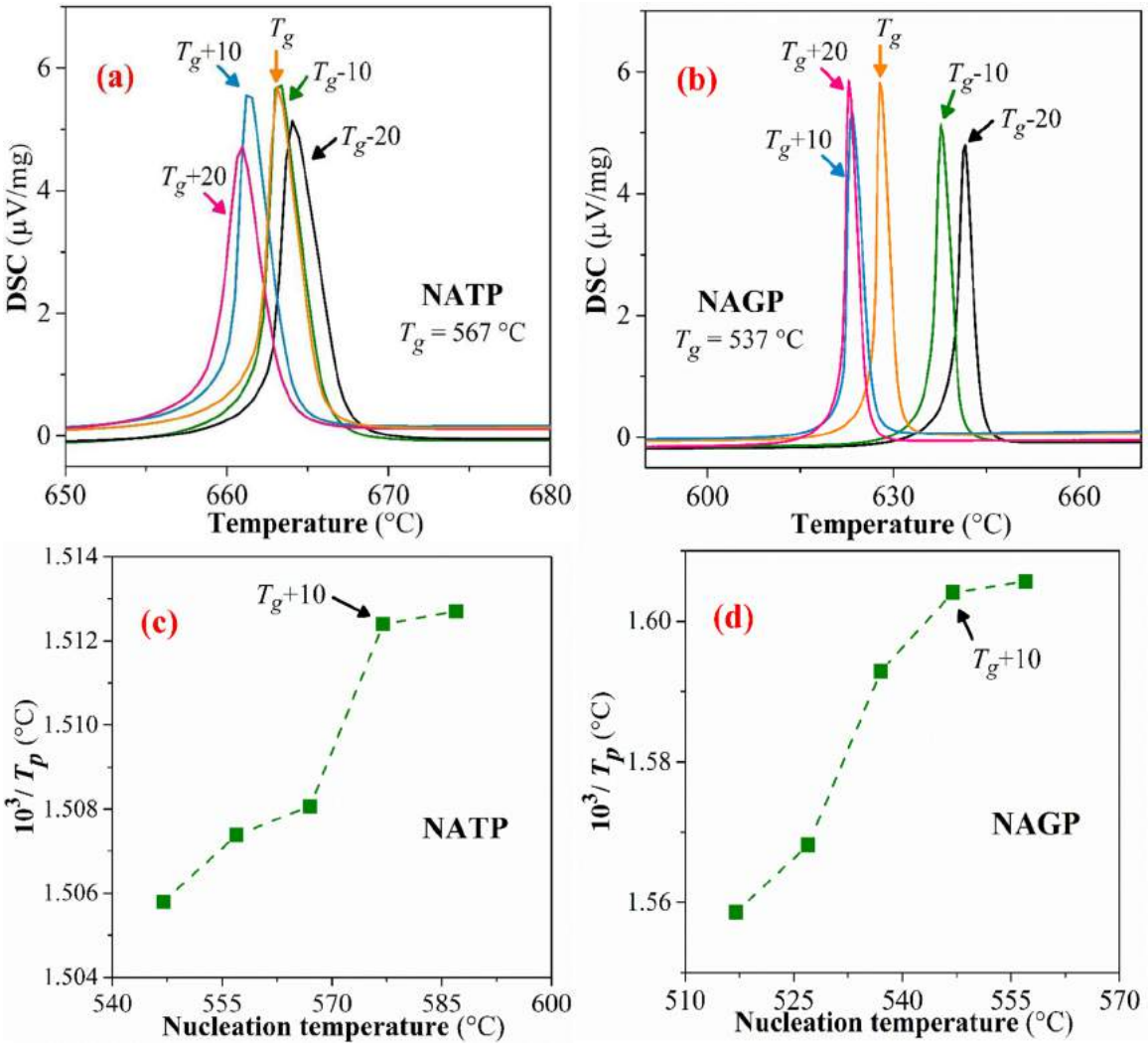

Fig. 2. DSC curves of (a) NATP and (b) NAGP samples nucleated for 30 min and 3 h respectively, at $T_g - 20$, $T_g - 10$, T_g, $T_g + 10$ and $T_g + 20$. Plot of the inverse of the crystallization peak temperature (T_p) vs. nucleation temperature for the (c) NATP and (d) NAGP glasses. The dotted lines in (c) and (d) are a guide to the eye. The uncertainties in (c) and (d) are less than the size of the square symbol. The error (~2 K) was estimated from DSC measurements performed in two glassy samples (from the same batch) at a heating rate of 10 °C/min.

card number ICSD 154069 was observed as the majority crystalline phase after SHT and DHT. Some peaks of the $Na_7(AlP_2O_7)_4PO_4$ spurious phase (ICSD 261924) were also observed in samples obtained by SHT with times ≥ 3 h (see Fig. 3). The percentage of this secondary phase is low (around 4 wt% for S3 and S6 samples). In sample crystallized at 700 °C (S700), this secondary phase is no longer seen due to its metastable nature [26]. Instead, the presence of around 8 wt% of the $AlPO_4$ phase (ICSD 280307) is observed, as calculated by the Rietveld refinement.

In Table 2, no significant variations in lattice cell parameters of the NASICON structure were observed in NATP and NAGP glass-ceramics, except for the S700 sample of the NAGP composition. In this sample, a decrease in the "*a*" parameter can be observed, which causes a contraction in the NASICON unit-cell volume. Ortiz-Mosquera et al. [26] showed that high percentage of secondary phases in $Na_{1+x}Al_xGe_{2-x}(PO_4)_3$ glass-ceramics are due to a dealumination of the NASICON unit cell leading to a decrease in the *x* value in the NASICON formula. In this sense, results from Table 2 show that for NATP and NAGP glass-ceramics with a low percentage of secondary phases (≤ 4 wt%), the chemical composition of the NASICON phase is not affected, i.e., the *x* value does not change. However, for the NAGP S700 sample (with 8 wt % of $AlPO_4$), the decrease in the NASICON cell volume indicates its dealumination due to the formation of $AlPO_4$. Thus, the electrical characterization of this sample is not included in the present work, since we want to evaluate the influence of microstructural variation on the electrical conductivity of NATP and NAGP samples and not the influence of compositional changes.

3.4. Scanning electron microscopy

SEM micrographs of the fractured surface and photo-images of the most representative NATP and NAGP glass-ceramics are shown in Figs. 4 and 5, respectively. The average grain size was determined from SEM micrographs in both compositions and the results are shown in Fig. 6.

Fig. 4 shows that NATP glass-ceramics exhibit asymmetric grains regardless of the type of heat treatment adopted and a dense microstructure except in the sample crystallized at 750 °C. The sample obtained by SHT at 850 °C (S850) (not shown in Fig. 4) also exhibited similar porosity. According to Watanabe et al. [28], the porosity in glass-ceramics appears due to the density difference between the precursor glass and the crystalline material. On the other hand, Table 2 shows the experimental densities of the NATP single-phase glass-ceramics determined by the Archimedes' principle using water ($\rho_{exp\text{-}w}$) and

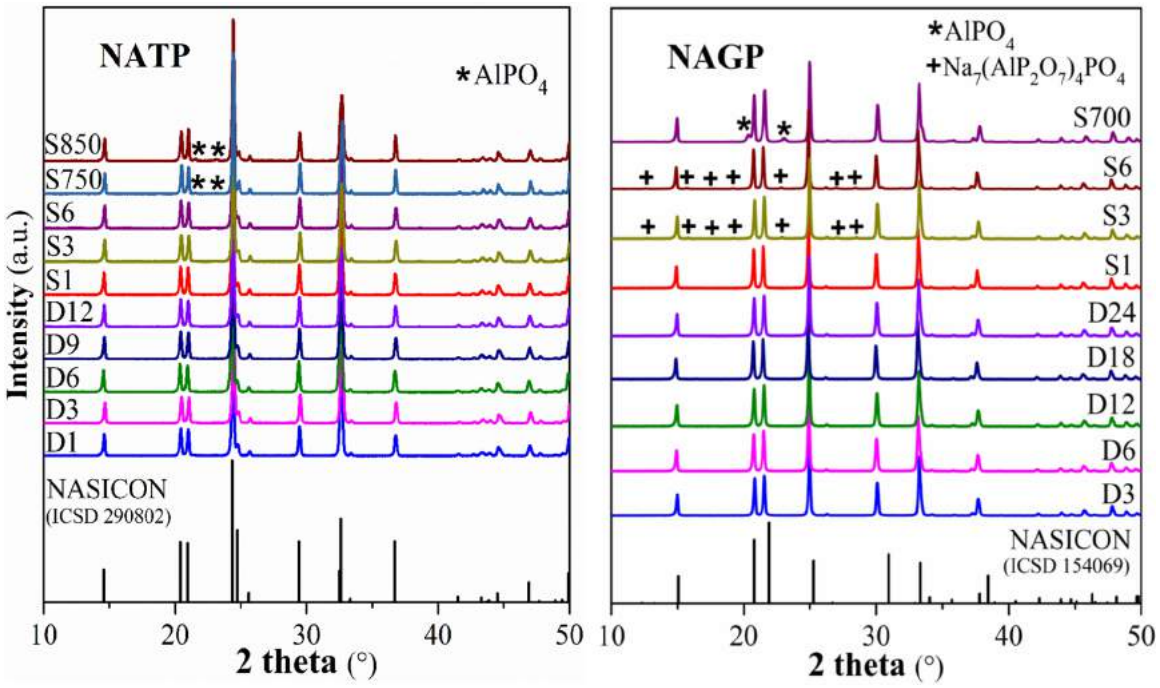

Fig. 3. X-ray diffractograms of NATP (left) and NAGP (right) glass-ceramics obtained by SHT and DHT, according to heat-treatment protocols summarized in Table 1.

ethanol ($\rho_{exp\text{-}e}$) as immersion fluids. It is interesting to note that, despite the presence of P_2O_5 in sample´s composition, the experimental densities did not vary significantly when measured with water or ethanol. The dense microstructures, observed in the NATP micrographs, are in good agreement with the experimental density measurements, which are higher than 95 % of the theoretical density (ρ_{th}). Due to the presence of spurious phases, experimental densities were not determined for the S750 and S850 samples (see Fig. 3).

Concerning the NAGP samples, the grains are better shaped as compared to the titanium-containing composition, with right angles and well-formed cubes (see Fig. 5). Note that for the S1 glass-ceramics in both compositions (more noticeable in NAGP), the grains are not fully formed, probably because the heat treatment time was not enough for the total crystallization in the chosen temperature. Better formed grains can be seen in samples treated for a longer time (S3 and S6). In fact, the slight decrease in the experimental density from samples S3 to S1 (Table 2) could suggest the presence of a small remaining glassy phase. It is also interesting to note that there is no evidence of the glassy phase on the X-ray diffractogram of these S1 samples (Fig. 3), suggesting that, if any, the glassy phase in these samples is present at a very low amount.

On the other hand, as can be seen in Fig. 6, glass-ceramics obtained by SHT for 1 h (S1) exhibit larger grains than those obtained by DHT in both compositions. This result is expected since the percentage of the

Table 2
Lattice parameters ($a = b$, c), unit cell volume (V) of the NASICON structure, theoretical density (ρ_{th}) and the agreement factor (R_{wp}) obtained by Rietveld refinement for NATP and NAGP glass-ceramic samples. Experimental density of glass-ceramics using water ($\rho_{exp\text{-}w}$) and ethanol ($\rho_{exp\text{-}e}$) as fluid. Mathematical errors given by TOPAS software are indicated between parentheses and for $\rho_{exp\text{-}w}$ and $\rho_{exp\text{-}e}$, this number corresponds to the standard deviation of five measurements performed in the same sample.

Composition	Heat treatment	Sample	a (Å)	c (Å)	V (Å^3)	ρ_{th} (g/cm^3)	$\rho_{exp\text{-}w}$ (g/cm^3)	$\rho_{exp\text{-}e}$ (g/cm^3)	$\rho_{exp\text{-}e}/\rho_{th}$ (%)	R_{wp}* (%)
		S1	8.4749(6)	21.597(2)	1343.3(2)	2.9922(4)	2.82(2)	2.86(1)	95.58	9.98
		S3	8.4752(5)	21.608(1)	1344.1(2)	2.9905(4)	2.86(1)	2.87(3)	95.97	9.74
	SHT	S6	8.4738(6)	21.614(2)	1344.1(2)	2.9906(4)	2.91(1)	2.94(1)	98.30	9.61
		S750	8.4826(3)	21.551(1)	1342.9(1)	–	–	–	–	10.28
NATP		S850	8.4825(7)	21.579(1)	1344.7(1)	–	–	–	–	10.84
		D1	8.4733(5)	21.605(2)	1343.4(2)	2.9922(4)	2.84(2)	2.88(2)	96.25	9.92
		D3	8.4750(6)	21.590(2)	1343.0(2)	2.9931(4)	2.82(1)	2.94(4)	98.22	10.24
	DHT	D6	8.4730(6)	21.605(2)	1343.3(2)	2.9923(4)	2.91(3)	2.93(2)	97.91	9.76
		D9	8.4716(7)	21.623(2)	1343.9(2)	2.9907(5)	2.86(4)	2.88(1)	96.29	9.82
		D12	8.4743(5)	21.602(1)	1343.5(2)	2.9919(4)	2.86(2)	2.89(1)	96.59	10.04
		S1	8.2888(2)	21.3892(5)	1272.66(7)	3.323(5)	3.07(2)	3.03(2)	91.18	10.11
	SHT	S3	8.2806(2)	21.3903(5)	1270.21(6)	3.332(4)	3.04(1)	3.08(1)	92.44	8.98
		S6	8.2863(2)	21.3927(5)	1272.09(5)	–	–	–	–	8.76
NAGP		S700	8.2470(2)	21.3994(6)	1260.46(7)	–	–	–	–	9.78
		D3	8.2877(2)	21.4001(5)	1272.96(6)	3.317(4)	3.11(2)	3.12(2)	94.06	8.94
		D6	8.2793(2)	21.4145(5)	1271.23(6)	3.324(4)	3.13(3)	3.10(2)	93.26	8.81
	DHT	D12	8.2798(2)	21.4115(6)	1271.21(7)	3.324(4)	3.09(1)	3.08(1)	92.66	9.84
		D18	8.2868(2)	21.401045)	1272.73(5)	3.317(4)	3.09(2)	3.10(1)	93.46	8.59
		D24	8.2818(2)	21.4169(5)	1272.14(6)	3.319(4)	3.22(4)	3.19(3)	96.11	8.91

* $R_{wp} = \Sigma\,[w(y_o - y_c)^2 / \Sigma\, w y_o^2]^{1/2}$; y_o = Observed intensity, y_c = Calculated intensity, $w = 1/y_o$.

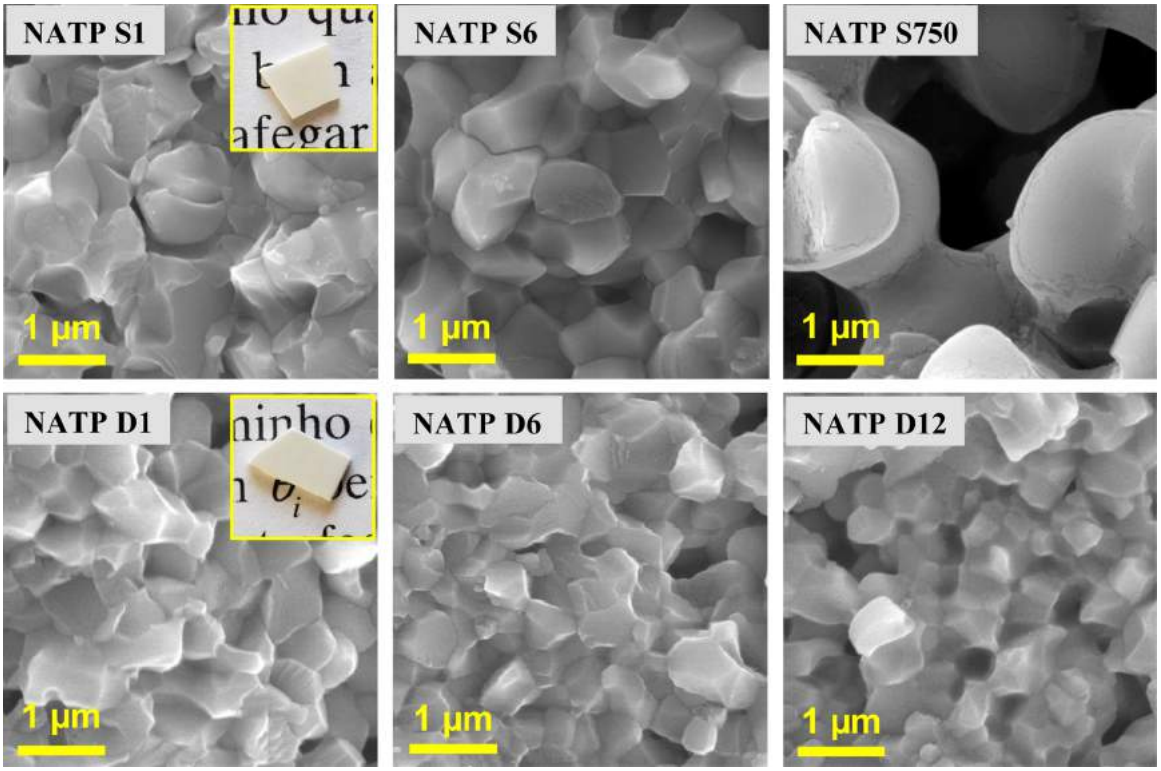

Fig. 4. SEM micrographs and photo-images of NATP glass-ceramics obtained by SHT and DHT, according to heat-treatment protocols summarized in Table 1.

nuclei present before the crystallization step in S1 samples is much lower than that of samples crystallized by two steps (DHT). In other words, the nuclei to be transformed into grains are more separated between them and its growth is less limited in the S1 samples. Fig. 6 shows a tendency to decrease the average grain size with the increase in the nucleation time in DHT for both compositions. As expected, longer nucleation times favor the density of nuclei, and thus the final grain size is limited by the grains which impinge each other as the growth process occurs.

In Fig. 6, the average grain size in S1, S3 and S6 samples of NATP remains constant within the error bar, with increasing time in the crystallization heat-treatment performed at 630 °C. Different behavior

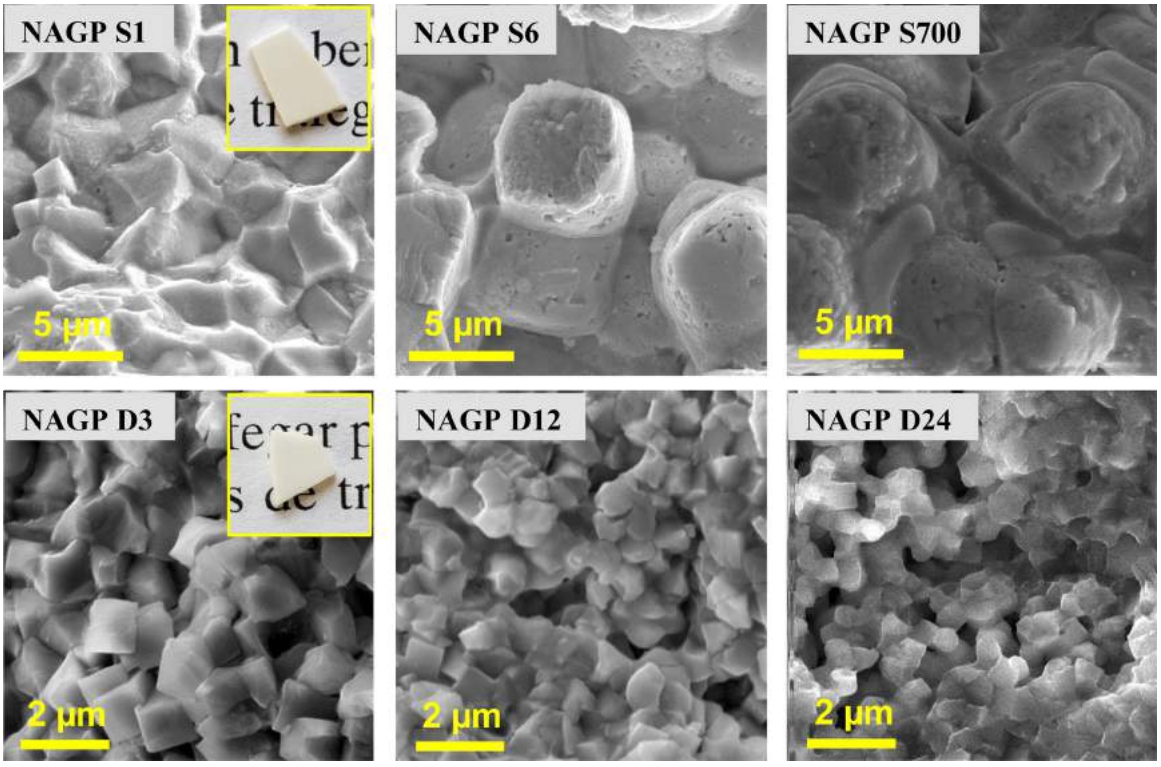

Fig. 5. SEM micrographs and photo-images of NAGP glass-ceramics obtained by SHT and DHT, according to heat-treatment protocols summarized in Table 1.

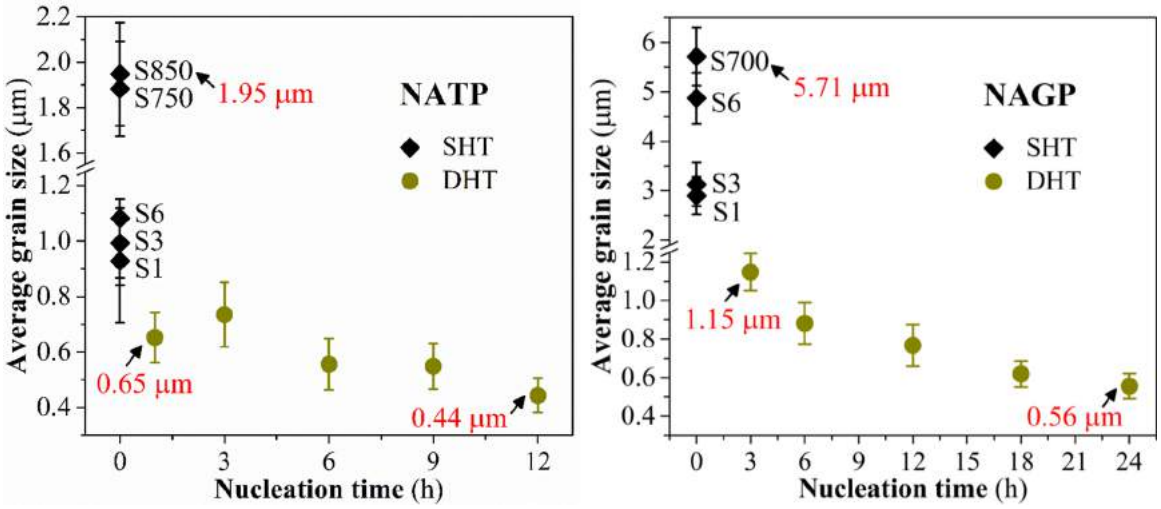

Fig. 6. Evolution of the average grain size as a function of the nucleation time in NATP (left) and NAGP (right) glass-ceramics obtained from SHT and DHT. See Table 1 for sample acronyms. The error bar indicates the standard deviation from the measurement of 50 grains.

is observed in the NAGP samples crystallized by SHT at 600 °C (S1, S3, and S6), where a noticeable grain growth is observed in the sample treated for 6 h (S6). In addition, it is seen that the increase in the temperature of SHT promotes an increment in the average grain size of up to 2 times in both compounds (for the same crystallization time).

In summary, SEM results show that the smallest and largest grain sizes are 0.443 µm (D12) and 1.948 µm (S850) for NATP, and 0.556 µm (D24) and 5.713 µm (S700) for NAGP, respectively. It is important to note that the variations in grain size exhibited by the compounds NAGP and NATP are greater than those reported by Cruz et al. [4] and Narváez-Semanate et al. [6] in Li^+-ion conducting analogous glass-ceramics. In the case of $Li_{1.3}Al_{0.3}Ti_{1.7}(PO_4)_3$ compound, the average grain size changed between ~ 110 nm and 380 nm with the variation of the heat treatment protocol while in the $Li_{1.5}Al_{0.5}Ge_{1.5}(PO_4)_3$, the grain size varied from 220 nm to 8 µm. This finding is quite interesting and will be discussed in the following section on the electrical characterization.

3.5. Complex impedance spectroscopy

Fig. 7a,b shows, as examples, the Nyquist plots (-*Z*″ vs. *Z*′) obtained at 100 °C from the samples treated with the shortest (1 h for NATP and 3 h for NAGP) and longest (12 h for NATP and 24 h for NAGP) nucleation times. Similar impedance plots (not shown here) were obtained for the other glass-ceramics obtained by DHT and SHT.

It can be seen in Fig. 7a,b that an increase in the nucleation time leads to an increment in the total resistivity, read at the low-frequency intersection of the impedance semi-circle with the *Z*′ axis. At the lowest frequencies, a straight line is also observed that indicates the blockage of the ions in the electrodes, which also confirms the ionic nature of electrical conductivity in NATP and NAGP glass-ceramics. This behavior is in good agreement with the results reported in our previous works on the $Na_{1+x}Al_xTi_{2-x}(PO_4)_3$ and $Na_{1+x}Al_xGe_{2-x}(PO_4)_3$ NASICON series [5,18].

Fig. 7a also shows the formation of a semicircle in the high-frequency region (at MHz frequencies), as well as the presence of a shoulder in the mid-frequency zone (at kHz frequencies) for the D1 and D12 NATP samples. Each of these semicircles is associated with the grain and grain boundary contribution, respectively, as indicated in the Nyquist plots. Fig. 7a reveals that the size of the second (mid-frequency) semicircle, associated with the grain boundary component, increases with the nucleation time, i.e., with the decrease in the average grain size (Fig. 6). This behavior in the -*Z*″ vs. *Z*′ plots is expected since the D12 sample has a higher grain boundary volume fraction, which is caused by the smaller average grain size, than the D1 glass-ceramic (see Section 3.4) [29–31]. In fact, the increase in the r_{gb} / (r_{gb} + r_g) ratio (see Table 3), also called the blocking effect [31], calculated from the diameter associated with the grain (r_g) and grain boundary (r_{gb}), also confirms this idea. In the case of the NAGP samples, it was not possible to separate the grain and the grain boundary contribution since the Nyquist diagram (Fig. 7b) shows a single semicircle for SHT and DHT glass-ceramics. Thus, the semicircle in the -*Z*″ vs. *Z*′ plot was associated with the sum of both contributions.

The total conductivity (σ_t) of NATP and NAGP glass-ceramics were calculated from the inverse of the total resistivity measured in the temperature range from 50–300 °C. In addition, the classical equivalent circuit model shown in Fig. 7f was used to determine the grain (R_g) and grain boundary (R_{gb}) resistances from the Nyquist plots of the NATP composition. In this circuit, the constant phase elements are used to simulate the non-ideal capacitance of these two contributions (CPE_g and CPE_{gb}) and also, the behavior of electrode-sample interface (CPE_{el}). The analysis of grain and grain boundary contributions was limited to the 50–130 °C temperature range since for higher temperatures, the semicircles in the Nyquist plots were not well resolved. The expression $\sigma_i = l/(R_iA)$) (i = g, gb^m) was used to calculate the grain (σ_g) and macroscopic grain boundary ($\sigma_{gb}{}^m$) conductivities. Furthermore, the specific grain boundary conductivity ($\sigma_{gb}{}^{sp}$) was determined by the Brick Layer Model using Eq. (1) [32,33]:

$$\sigma_{gb}{}^{sp} = (l/R_{gb}A)(d/D) \quad (1)$$

where l is the sample thickness, A is the area of the sample, d is the grain boundary thickness and D is the average grain size. The $\sigma_{gb}{}^{sp}$ represents the real conductivity of the grain boundary since it is not influenced by microstructural factors, i.e., grain size variations [34]. In addition, since $\sigma_{gb}{}^m = l/R_{gb}A$ as mentioned above, the macroscopic and specific grain boundary conductivities are related by the following expression:

$$\sigma_{gb}{}^m = \sigma_{gb}{}^{sp}(D/d) \quad (2)$$

By analyzing Eq. (2), it can be noted that the macroscopic grain boundary conductivity could be enhanced either by improving the specific grain boundary conductivity, by the increase of the grain size or by the decrease of the grain boundary thickness [33].

On the other hand, considering the assumption that the grain and grain boundary permittivity is similar, we determined the grain boundary thickness from Eq. (3) [35]:

$$d = D(C_g/C_{gb}) \quad (3)$$

where C_g and C_{gb} are the grain and grain boundary capacitances,

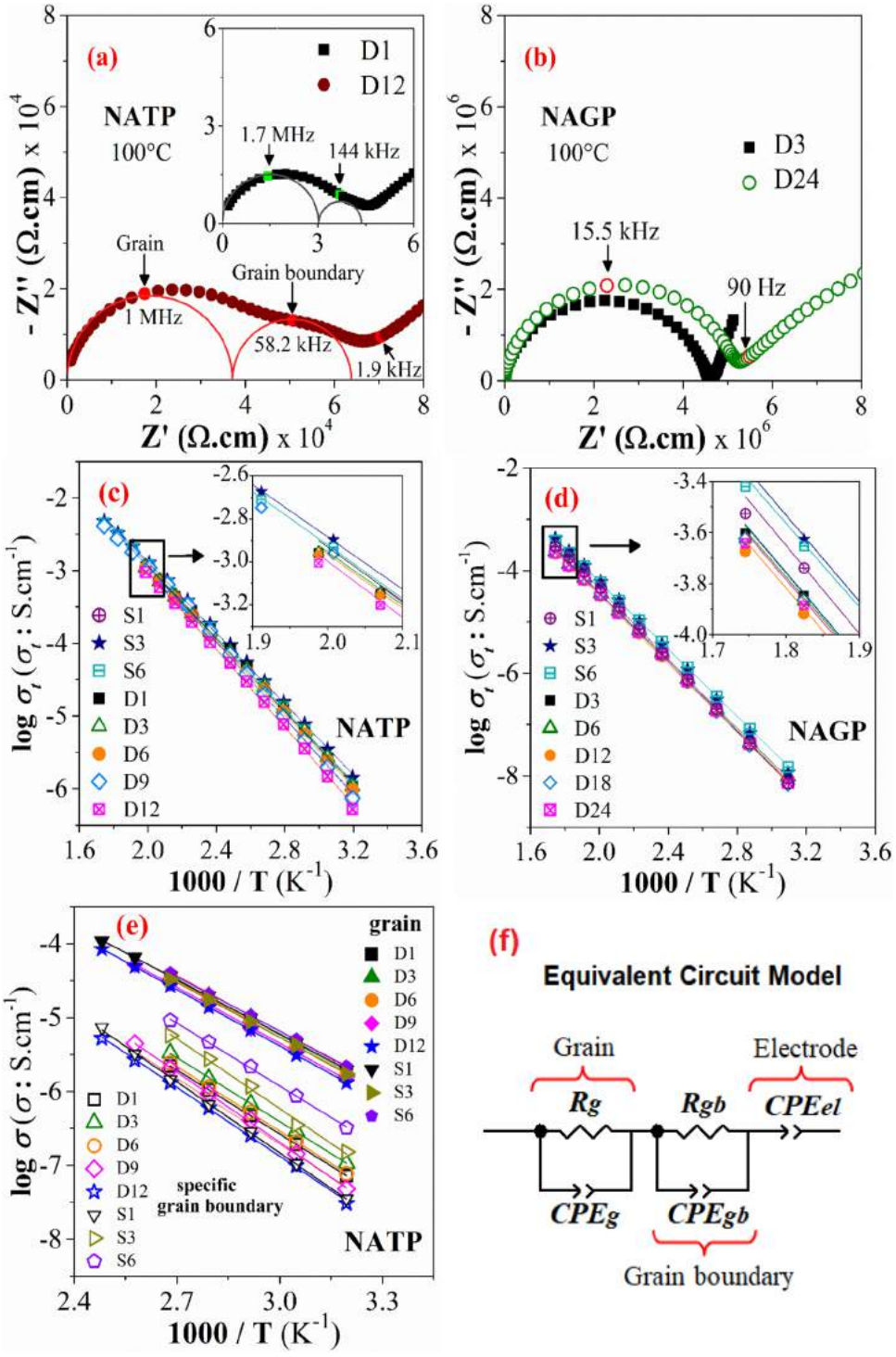

Fig. 7. Nyquist plots of (a) NATP and (b) NAGP glass-ceramics obtained by DHT according to the heat-treatment protocols summarized in Table 1. Temperature dependence of total ionic conductivity (σ_t) in the (c) NATP and (d) NAGP glass-ceramics. (e) Arrhenius plot of grain and specific grain boundary of NATP glass-ceramics. (f) Equivalent circuit model used to analyze the Nyquist plots in (a). The solid lines in the Arrhenius and Nyquist plots represent the linear fitting and the circuit fitting, respectively.

respectively.

The dependence of the total, grain, and specific grain boundary conductivity with the inverse of temperature (Arrhenius plot) for NAGP and NATP samples are shown in Fig. 7c–e. The total (E_a), grain (E_{a-g}), and grain boundary ($E_{a-gb}{}^{sp}$ and $E_{a-gb}{}^{m}$) activation energy values were calculated by the assumption of an Arrhenius behavior (see Eq. (4)). These values are summarized in Table 3 together with the ionic conductivity at 100 °C for all contributions.

$$\log\sigma = \log\sigma_o - 2.3\,E_a\ /\ k_B T \quad (4)$$

As shown in Table 3, the values of the logarithm of the pre-exponential factor for the total conductivity (log σ_0) are around 2 (which is a typical value for ionic conductors [5,36]) except for the NATP samples obtained at higher temperatures (S750 and S850). In fact, these glass-ceramics exhibit the lowest log σ_0 from all the samples analyzed. As reported by Mariappan et al. [37], low values of the pre-exponential

Table 3
Activation energy of total (E_a), grain (E_{a-g}), specific ($E_{a-gb}{}^{sp}$) and macroscopic ($E_{a-gb}{}^{m}$) grain boundary conductivity. Conductivities at 100 °C for the grain (σ_{g-100}), specific ($\sigma_{gb}{}^{sp}{}_{-100}$) and microscopic grain boundary ($\sigma_{gb}{}^{m}{}_{-100}$) of NATP samples and total ionic conductivity at 100 °C ($\sigma_{t-100°C}$) for NATP and NAGP glass-ceramics obtained by SHT and DHT. Numbers between parentheses represent the mathematical uncertainty in the final digit. The ratio $r_{gb}/(r_g+r_{gb})$ and the thickness of the grain boundary, d (calculated by Eq. (3)) are shown on the right.

Comp[1]	HT[2]	Sample	Total			Grain		Specific grain boundary			Macroscopic grain boundary	$r_{gb}/(r_g+r_{gb})$	d
			E_a (eV)	log σ_0 (σ_0: S.cm^{-1})	$\sigma_{t-100°C}$ (S.cm^{-1})	E_{a-g} (eV)	σ_{g-100} (S.cm^{-1})	$E_{a-gb}{}^{sp}$ (eV)	$\sigma_{gb}{}^{sp}{}_{-100}$ (S.cm^{-1})	$E_{a-gb}{}^{m}$ (eV)	$\sigma_{gb}{}^{m}{}_{-100}$ (S.cm^{-1})		(nm)
		S1	0.685(4)	2.58(5)	2.1×10^{-7}	–	–	–	–	–	–	–	–
	SHT	S3	0.673(2)	2.30(3)	3.1×10^{-7}	–	–	–	–	–	–	–	–
		S6	0.650(3)	2.34(3)	3.6×10^{-7}	–	–	–	–	–	–	–	–
NAGP		D3	0.641(8)	2.07(9)	2.6×10^{-7}	–	–	–	–	–	–	–	–
		D6	0.648(4)	2.15(5)	2.5×10^{-7}	–	–	–	–	–	–	–	–
	DHT	D12	0.662(3)	2.19(4)	1.8×10^{-7}	–	–	–	–	–	–	–	–
		D18	0.669(4)	2.30(6)	1.8×10^{-7}	–	–	–	–	–	–	–	–
		D24	0.664(5)	2.24(6)	1.9×10^{-7}	–	–	–	–	–	–	–	–
		S1	0.513(6)	2.32(6)	2.4×10^{-5}	0.489(3)	3.7×10^{-5}	0.66(1)	2.0×10^{-6}	0.64(1)	8.5×10^{-5}	0.29	21
		S3	0.494(5)	2.06(6)	2.5×10^{-5}	0.491(7)	3.4×10^{-5}	0.64(1)	7.5×10^{-6}	0.62(2)	9.1×10^{-5}	0.23	58
	SHT	S6	0.483(4)	2.01(4)	2.9×10^{-5}	0.489(2)	4.0×10^{-5}	0.56(1)	9.6×10^{-6}	0.56(2)	1.2×10^{-4}	0.26	65
		S750	0.487(2)	1.66(2)	1.2×10^{-5}	–	–	–	–	–	–	–	–
		S850	0.492(2)	1.87(3)	1.7×10^{-5}	–	–	–	–	–	–	–	–
NATP		D1	0.499(7)	2.10(9)	2.3×10^{-5}	0.494(3)	3.4×10^{-5}	0.66(1)	3.6×10^{-6}	0.57(0)*	8.0×10^{-5}	0.30	23
		D3	0.491(4)	2.00(6)	2.3×10^{-5}	0.502(7)	3.8×10^{-5}	0.65(2)	5.7×10^{-6}	0.57(0)*	8.1×10^{-5}	0.31	25
	DHT	D6	0.499(4)	2.07(6)	2.1×10^{-5}	0.506(1)	3.5×10^{-5}	0.67(1)	4.2×10^{-6}	0.58(0)*	6.9×10^{-5}	0.35	24
		D9	0.514(7)	2.24(8)	1.9×10^{-5}	0.499(4)	2.9×10^{-5}	0.65(2)	2.4×10^{-6}	0.63(0)*	6.7×10^{-5}	0.37	19
		D12	0.530(5)	2.34(7)	1.5×10^{-5}	0.503(1)	2.9×10^{-5}	0.67(1)	1.8×10^{-6}	0.62(0)*	3.8×10^{-5}	0.42	19

[1] Comp: Composition.
[2] HT: Heat treatment.
* The uncertainty is in the third decimal place.

factor can be expected when samples exhibit poor contact between grains. In our case, we believe that this poor contact in S750 and S850 glass-ceramics is probably caused by the presence of pores, as seen in Section 3.4.

Table 3 shows that the total ionic conductivities of NATP samples is two orders of magnitude higher than those exhibited for the NAGP glass-ceramics. This difference between conductivities is due to higher activation energies of NAGP samples. We attribute this behavior to the smaller bottleneck size of the NAGP NASICON structure, through which the Na^+ ions migrate within the material [18].

Fig. 8a–d illustrates the variation of the total ionic conductivity at 100 °C ($\sigma_{t-100°C}$) and total activation energy as a function of the grain size in NATP and NAGP samples. It can be noted in both compositions that the electrical conductivity tends to increase when the average grain size is increased. This improvement in ionic conductivity is up to two times in both compositions. We note that although remarkable variations in grain size were promoted in the NATP and NAGP compounds (as shown in Section 3.4), the increase in ionic conductivity was not of several orders of magnitude like those reported in the lithium-containing analogous series, $Li_{1+x}Al_xM_{2-x}(PO_4)_3$ (M = Ge, Ti) [4,6]. This result is intriguing, considering that in $Li_{1+x}Al_xM_{2-x}(PO_4)_3$ (M = Ge, Ti), the increase in grain size was less than that promoted in the present work.

On the other hand, Fig. 8a shows that the S750 and S850 samples (for NATP) do not exhibit the highest values of total ionic conductivity despite the fact that they exhibit the largest grain size and low activation energy (see Fig. 8c). This decrease in the ionic conductivity is attributed to the porosity, which promoted a decrease in the pre-exponential factor of the Arrhenius expression (Eq. 4). Thus, it can be argued that the low pre-exponential factor, log σ_0, prevailed over the slightly decreased activation energy in those samples. Regarding the NAGP S1 sample, the drop in the ionic conductivity value is expected since we suspect that a small amount of remaining glassy phase is still present after the crystallization treatment.

On the other hand, Fig. 8a,b also shows an improvement in the total ionic conductivity as the crystallization time increases (from S1 to S6) in samples obtained by SHT in both compositions. The highest ionic conductivity at 100 °C was reached at the samples crystallized by SHT for 6 h (S6) with values of 2.9×10^{-5} S. cm^{-1} and 3.6×10^{-7} S.cm^{-1} for NATP and NAGP, respectively (see Table 3).

Regarding glass-ceramics obtained by DHT, Fig. 8c,d shows an increase in the total activation energy (E_a) with the increase in the nucleation time, i.e., with the decrease in the average grain size, for NATP and NAGP. As can be seen in Fig. 8a,b, this increase in E_a promotes a decrease in the total conductivity of the samples.

Table 3 shows that the grain activation energy (E_{a-g}) of NATP glass-ceramics is similar (around 0.49 to 0.50 eV) regardless of the type of heat treatment, SHT or DHT, to which the sample was subjected. This result is expected mainly because the chemical composition (x amount) of samples is not affected by the heat treatment protocol (as analyzed by XRD in Section 3.3) and also because, as shown previously, the variation of grain size in NATP samples only affects the electrical properties of the grain boundary. We would like to suggest that the activation energy for the grain in the NAGP samples could also have similar values, regardless of the different heat treatment protocols, since the lattice parameters of the unit cell of those glass-ceramics are also constant (see Table 2). However, this hypothesis cannot be experimentally corroborated because it was not possible to analyze the electrical-microstructure relationship of the NAGP glass-ceramics.

Considering that no changes were observed in the grain contribution (E_{a-g}) of NATP samples, we were able to analyze the evolution of the total conductivity based on the grain boundary behavior. Table 3 shows that the intergranular region exhibits higher activation energies ($E_{a-gb}{}^{sp}$ and $E_{a-gb}{}^{m}$) than those observed for the grains. This indicates that, as expected, the Na^+ ions move with greater difficulty in the grain boundary. In fact, it is noted that the specific grain boundary conductivity at 100 °C ($\sigma_{gb}{}^{sp}{}_{-100}$) of NATP samples is one order lower than that exhibited by the grain.

On the other hand, Table 3 also shows an increment in the specific grain boundary conductivity at 100 °C ($\sigma_{gb}{}^{sp}{}_{-100}$) as the crystallization time increases (from S1 to S6) in the NATP samples obtained by SHT. Since changes in $\sigma_{gb}{}^{sp}$ are independent of the microstructural factors [34,35], we attributed the improvement of the $\sigma_{gb}{}^{sp}$ to the reduction of the glassy phase in samples treated at longer crystallization times (S6

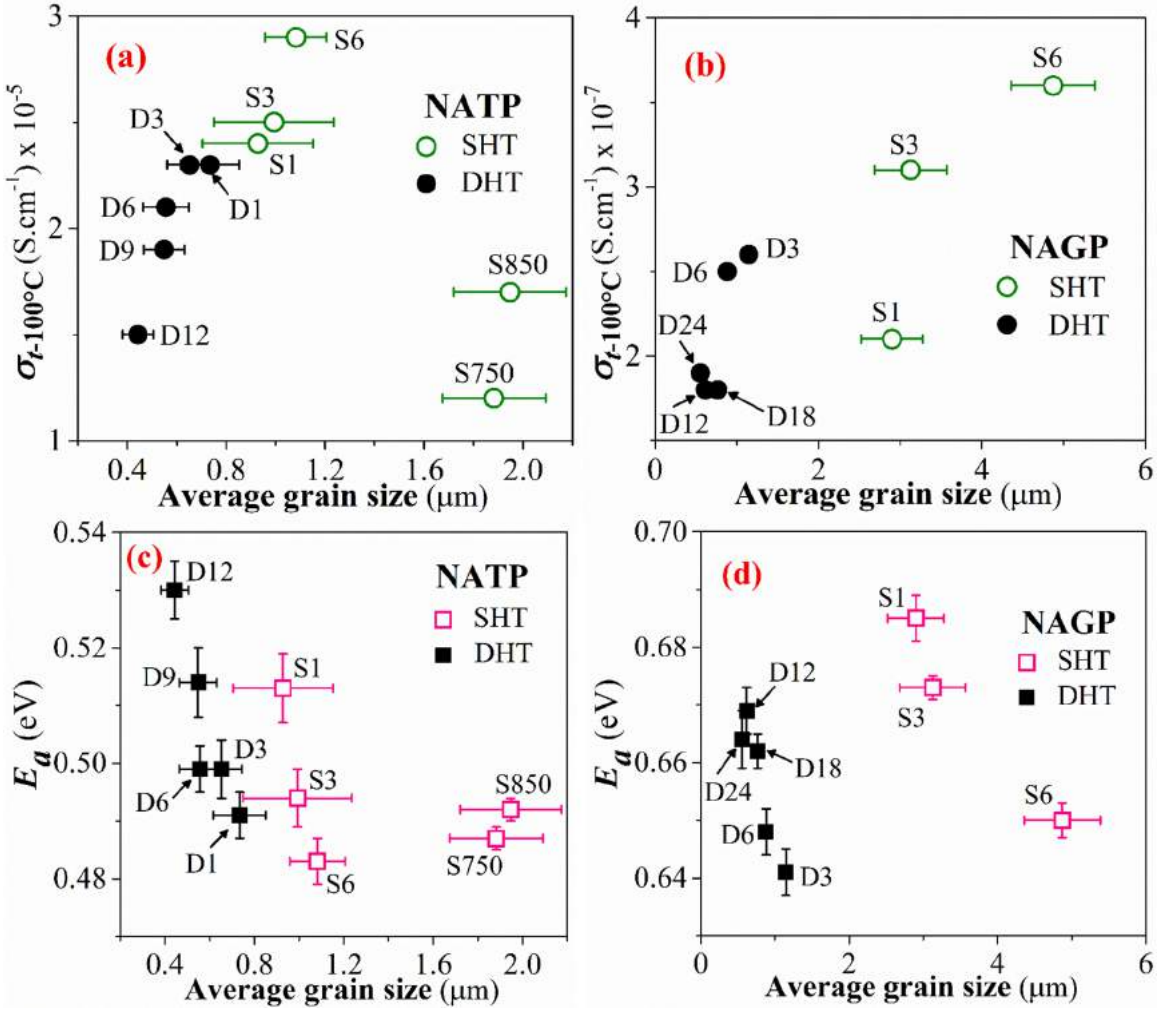

Fig. 8. (a) Total ionic conductivity at 100 °C ($\sigma_{t\text{-}100°C}$) as a function of the average grain size of (a) NATP and (b) NAGP samples. Activation energy for total ionic conductivity as a function of the average grain size of (c) NATP and (d) NAGP glass-ceramics.

sample). In fact, the increase in the relative density ($\rho_{exp\text{-}e}$ /ρ_{th}, see Table 2) from samples S1 to S6 also suggests an increase in crystallinity. Considering that the remaining glassy phase is usually located in the grain boundary region, its decrease would be reflected in the decrease in the activation energy of specific grain boundary conductivity ($E_{a\text{–}gb}{}^{sp}$). In addition, since no significant changes in the average grain size (D) were seen from S1 to S6, we can infer from Eq. 2 that the enhancement of macroscopic grain boundary conductivity ($\sigma_{gb}{}^{m}$) is mostly caused by an increase in $\sigma_{gb}{}^{sp}$, despite the increase observed in d (see Table 3).

Regarding NATP glass-ceramics obtained by DHT, Table 3 shows that no changes occur in the activation energy of specific grain boundary conductivity ($E_{a\text{–}gb}{}^{sp}$) when the nucleation time increases from D1 to D12. This behavior in $E_{a\text{–}gb}{}^{sp}$ can be understood by a similar degree of crystallization of these samples since they were treated at the same temperature and time of grain growth (see Table 1) [6]. Additionally, Table 3 shows that, with exception to sample D1, d tends to decrease with increased nucleation time. Moreover, analyzing Eq. (2), we note that the macroscopic grain boundary conductivity ($\sigma_{gb}{}^{m}$) is also affected by the variation of average grain size in the NATP samples crystallized by two-steps. In fact, Table 3 shows that samples with a smaller grain size (D12) exhibit lower values of $\sigma_{gb}{}^{m}$ than those with larger grains (D1–D3). It is worth mentioning that the influence of the grain size in the Na^+ conductivity of DHT samples is also reflected by the increase in the energy barrier of the macroscopic grain boundary ($E_{a\text{–}gb}{}^{m}$) with the decrease in the grain size.

4. Conclusions

We synthesized NASICON glass-ceramics from single (SHT) and double (DHT) crystallization heat treatments performed on NATP and NAGP parent glasses. By DSC, it was estimated that the temperature in which occurs the maximum nucleation rate corresponds to T_g + 10 in both precursor glasses. SEM micrographs show that the different heat treatment protocols applied in this work are effective to obtain materials with different average grain sizes (from the nanometer to the micrometer scale). For both compositions, samples crystallized by one-step heat treatments exhibited larger grains than those obtained by two-steps. Regarding samples obtained by DHT, as the nucleation time increased, the grain size decreased. The impedance spectroscopy results show that the total ionic conductivity of NATP and NAGP samples can be increased up to two times due to the microstructural variations. In this sense, contrary to previous studies on the lithium-containing analogous series, we noted that remarkable variations in grain size do not promote an increase in orders of magnitude in the total conductivity of NATP and NAGP sodium-ion containing samples. The highest total ionic conductivities at 100 °C are achieved in the glass-ceramics crystallized by SHT for 6 h in both compositions. From the analysis of grain and grain boundary contributions in the NATP samples, the increase of total conductivity is attributed to the improvement of the grain boundary conductivity. In addition, it was noted that the enhancement of electrical behavior of grain boundary is more influenced by the increase of specific grain boundary conductivity for samples obtained by SHT,

while in the DHT samples, the effect of the increase of the average grain size is more significant.

Declaration of Competing Interest

The authors declare that they have no known competing financial interests or personal relationships that could have appeared to influence the work reported in this paper.

Acknowledgments

The authors gratefully acknowledge the financial support of the Brazilian research funding agencies FAPESP (Fundação de Amparo à Pesquisa do Estado de São Paulo, Process No. 2013-07793, via the CEPID program) and CNPq (Conselho Nacional de Desenvolvimento Científico e Tecnológico, under Process No. 141220/2016-3 for AMNM and Process No. 168682/2017-6 for JFOM). This study was financed in part by the Coordenação de Aperfeiçoamento de Pessoal de Nível Superior - Brasil (CAPES) - Finance Code 001.

References

[1] J. Fu, Fast Li^+ ion conduction in Li_2O–Al_2O_3–TiO_2–SiO_2–P_2O_5 glass-ceramics, J. Am. Ceram. Soc. 80 (1997) 1901–1903, https://doi.org/10.1111/j.1151-2916.1997.tb03070.x.

[2] A. Sakamoto, S. Yamamoto, Glass-ceramics: engineering principles and applications, Int. J. Appl. Glas. Sci. 1 (2010) 237–247, https://doi.org/10.1111/j.2041-1294.2010.00027.x.

[3] E.D. Zanotto, A bright future for glass-ceramics, Am. Ceram. Soc. Bull. 89 (2010) 19–27.

[4] A.M. Cruz, E.B. Ferreira, A.C.M. Rodrigues, Controlled crystallization and ionic conductivity of a nanostructured $LiAlGePO_4$ glass-ceramic, J. Non-Cryst. Solids 355 (2009) 2295–2301, https://doi.org/10.1016/j.jnoncrysol.2009.07.012.

[5] J.F. Ortiz-Mosquera, A.M. Nieto-Muñoz, A.C.M. Rodrigues, Precursor glass stability, microstructure and ionic conductivity of glass-ceramics from the $Na_{1+x}Al_xGe_{2-x}(PO_4)_3$ NASICON series, J. Non-Cryst. Solids 513 (2019) 36–43, https://doi.org/10.1016/j.jnoncrysol.2019.03.008.

[6] J.L. Narváez-Semanate, A.C.M. Rodrigues, Microstructure and ionic conductivity of $Li_{1+x}Al_xTi_{2-x}(PO_4)_3$ NASICON glass-ceramics, Solid State Ionics 181 (2010) 1197–1204, https://doi.org/10.1016/j.ssi.2010.05.010.

[7] J. Deubener, M. Allix, M.J. Davis, A. Duran, T. Höche, T. Honma, T. Komatsu, S. Krüger, I. Mitra, R. Müller, S. Nakane, M.J. Pascual, J.W.P. Schmelzer, E.D. Zanotto, S. Zhou, Updated definition of glass-ceramics, J. Non-Cryst. Solids 501 (2018) 3–10, https://doi.org/10.1016/j.jnoncrysol.2018.01.033.

[8] V.M. Fokin, E.D. Zanotto, N.S. Yuritsyn, J.W.P. Schmelzer, Homogeneous crystal nucleation in silicate glasses: a 40 years perspective, J. Non-Cryst. Solids 352 (2006) 2681–2714, https://doi.org/10.1016/j.jnoncrysol.2006.02.074.

[9] N. Karpukhina, R.G. Hill, R.V. Law, Crystallisation in oxide glasses – a tutorial review, Chem. Soc. Rev. 43 (2014) 2174–2186, https://doi.org/10.1039/C3CS60305A.

[10] V.M. Fokin, A.A. Cabral, R.M.C.V. Reis, M.L.F. Nascimento, E.D. Zanotto, Critical assessment of DTA–DSC methods for the study of nucleation kinetics in glasses, J. Non-Cryst. Solids 356 (2010) 358–367, https://doi.org/10.1016/j.jnoncrysol.2009.11.038.

[11] O. Peitl, E.D. Zanotto, F.C. Serbena, L.L. Hench, Compositional and microstructural design of highly bioactive P_2O_5–Na_2O–CaO–SiO_2 glass-ceramics, Acta Biomater. 8 (2012) 321–332, https://doi.org/10.1016/j.actbio.2011.10.014.

[12] Y. Liu, J. Liu, Q. Sun, D. Wang, K.R. Adair, J. Liang, C. Zhang, L. Zhang, S. Lu, H. Huang, X. Song, X. Sun, Insight into the microstructure and ionic conductivity of cold sintered NASICON solid electrolyte for solid-state batteries, ACS Appl. Mater. Interfaces 11 (2019) 27890–27896, https://doi.org/10.1021/acsami.9b08132.

[13] J.A. Dawson, P. Canepa, T. Famprikis, C. Masquelier, M.S. Islam, Atomic-scale influence of grain boundaries on Li-ion conduction in solid electrolytes for all-solid-state batteries, J. Am. Chem. Soc. 140 (2018) 362–368, https://doi.org/10.1021/jacs.7b10593.

[14] S. Randau, D.A. Weber, O. Kötz, R. Koerver, P. Braun, A. Weber, E. Ivers-Tiffée, T. Adermann, J. Kulisch, W.G. Zeier, F.H. Richter, J. Janek, Benchmarking the performance of all-solid-state lithium batteries, Nat. Energy 5 (2020) 259–270, https://doi.org/10.1038/s41560-020-0565-1.

[15] Z. Zhang, Y. Shao, B. Lotsch, Y.-S. Hu, H. Li, J. Janek, L.F. Nazar, C.-W. Nan, J. Maier, M. Armand, L. Chen, New horizons for inorganic solid state ion conductors, Energy Environ. Sci. 11 (2018) 1945–1976, https://doi.org/10.1039/C8EE01053F.

[16] M.I. Jamesh, A.S. Prakash, Advancement of technology towards developing Na-ion batteries, J. Power Sources 378 (2018) 268–300, https://doi.org/10.1016/j.jpowsour.2017.12.053.

[17] P.K. Nayak, L. Yang, W. Brehm, P. Adelhelm, From lithium-ion to sodium-ion batteries: advantages, challenges, and surprises, Angew. Chem. Int. Ed. 57 (2018) 102–120, https://doi.org/10.1002/anie.201703772.

[18] A.M. Nieto-Muñoz, J.F. Ortiz-Mosquera, A.C.M. Rodrigues, The role of Al^{+3} on the microstructural and electrical properties of $Na_{1+x}Al_xTi_{2-x}(PO_4)_3$ NASICON glass-ceramics, J. Alloys. Compd. 820 (2020) 153148, , https://doi.org/10.1016/j.jallcom.2019.153148.

[19] C.S. Ray, D.E. Day, Determining the nucleation rate curve for lithium disilicate glass by differential thermal analysis, J. Am. Ceram. Soc. 73 (1990) 439–442, https://doi.org/10.1111/j.1151-2916.1990.tb06532.x.

[20] Oxford Cryosystems, Crystallographica search-match, J. Appl. Crystallogr. 32 (1999) 379–380, https://doi.org/10.1107/S0021889899004124.

[21] A.A. Coelho, J. Evans, I. Evans, A. Kern, S. Parsons, The TOPAS symbolic computation system, Powder Diffr. 26 (2011) S22–S25, https://doi.org/10.1154/1.3661087.

[22] A. Belsky, M. Hellenbrandt, V.L. Karen, P. Luksch, New developments in the Inorganic Crystal Structure Database (ICSD): accessibility in support of materials research and design, Acta Crystallogr. Sec. B Struct. Sci. B 58 (2002) 364–369, https://doi.org/10.1107/S0108768102006948.

[23] C.A. Schneider, W.S. Rasband, K.W. Eliceiri, NIH image to ImageJ: 25 years of image analysis, Nat. Methods 9 (2012) 671–675, https://doi.org/10.1038/nmeth.2089.

[24] C.S. Ray, D.E. Day, Identifying internal and surface crystallization by differential thermal analysis for the glass-to-crystal transformations, Thermochim. Acta 280–281 (1996) 163–174, https://doi.org/10.1016/0040-6031(95)02640-1.

[25] E.D. Zanotto, Isothermal and adiabatic nucleation in glass, J. Non-Cryst. Solids 89 (1987) 361–370, https://doi.org/10.1016/S0022-3093(87)80278-8.

[26] J.F. Ortiz-Mosquera, A.M. Nieto-Muñoz, H. Bradtmüller, H. Eckert, A.C.M. Rodrigues, Isothermal evolution of phase composition, structural parameters, and ionic conductivity in $Na_{1+x}Al_xGe_{2-x}(PO_4)_3$ glass-ceramics, J. Non-Cryst. Solids 533 (2020) 119725, , https://doi.org/10.1016/j.jnoncrysol.2019.119725.

[27] A.M. Nieto-Muñoz, J.F. Ortiz-Mosquera, A.C.M. Rodrigues, Novel sodium superionic conductor of the $Na_{1+y}Ti_2Si_yP_{3-y}O_{12}$ series for application as solid electrolyte, Electrochim. Acta 319 (2019) 922–932, https://doi.org/10.1016/j.electacta.2019.07.032.

[28] A. Watanabe, M. Mitsudou, S. Kihara, Y. Abe, Preparation of void-free calcium phosphate glass-ceramics, J. Am. Ceram. Soc. 72 (1989) 1499–1500, https://doi.org/10.1111/j.1151-2916.1989.tb07687.x.

[29] J.H. Hwang, D.S. Mclachlan, T.O. Mason, Brick layer model analysis of nanoscale-to-microscale cerium dioxide, J. Electroceram. 3 (1999) 7–16, https://doi.org/10.1023/A:1009998114205.

[30] N.J. Kidner, Z.J. Homrighaus, B.J. Ingram, T.O. Mason, E.J. Garboczi, Impedance/dielectric spectroscopy of electroceramics-part 1: evaluation of composite models for polycrystalline ceramics, J. Electroceram. 14 (2005) 283–291, https://doi.org/10.1007/s10832-005-0969-0.

[31] M. Kleitz, M.C. Steil, Microstructure blocking effects versus effective medium theories in YSZ, J. Eur. Ceram. Soc. 17 (1997) 819–829, https://doi.org/10.1016/S0955-2219(97)89966-9.

[32] E. Barsoukov, J.R. Macdonald, Impedance Spectroscopy: Theory, Experiment, and Applications, John Wiley & Sons, Inc., Hoboken, NJ, USA, 2018, https://doi.org/10.1002/9781119381860.

[33] T. Van Dijk, A.J. Burggraaf, Grain boundary effects on ionic conductivity in ceramic $Gd_xZr_{1-x}O_{2-(x/2)}$ solid solutions, Phys. Status Solidi 63 (1981) 229–240, https://doi.org/10.1002/pssa.2210630131.

[34] L. Ge, R. Li, S. He, H. Chen, L. Guo, Enhanced grain-boundary conduction in polycrystalline $Ce_{0.8}Gd_{0.2}O_{1.9}$ by zinc oxide doping: scavenging of resistive impurities, J. Power Sources 230 (2013) 161–168, https://doi.org/10.1016/j.jpowsour.2012.12.084.

[35] J. Tao, A. Dong, J. Wang, The influence of microstructure and grain boundary on the electrical properties of scandia stabilized zirconia, Mater. Trans. 54 (2013) 825–832, https://doi.org/10.2320/matertrans.M2012385.

[36] M.L.F. Nascimento, A.C.M. Rodrigues, J.L. Souquet, Microscopic and thermodynamic interpretations of experimental data on ionic conductivity in lithium silicate glasses, Phys. Chem. Glas. Eur. J. Glas. Sci. Technol. Part B 51 (2010) 69–77.

[37] C.R. Mariappan, C. Yada, F. Rosciano, B. Roling, Correlation between microstructural properties and ionic conductivity of $Li_{1.5}Al_{0.5}Ge_{1.5}(PO_4)_3$ ceramics, J. Power Sources 196 (2011) 6456–6464, https://doi.org/10.1016/j.jpowsour.2011.03.065.